Controllable TiO_2 core-shell phase heterojunction for efficient photoelectrochemical water splitting under solar light

Ning Wei[a,b], Ying Liu[b,**], Min Feng[b,c], Zhaoxia Li[a], Shougang Chen[b], Youbin Zheng[a,c], Daoai Wang[a,c,*]

[a] State Key Laboratory of Solid Lubrication, Lanzhou Institute of Chemical Physics, Chinese Academy of Sciences, Lanzhou 730000, China
[b] Institute of Materials Science and Engineering, Ocean University of China, Qingdao 266100, China
[c] Qingdao Center of Resource Chemistry and New Materials, Qingdao 266100, China

A B S T R A C T

In this study, hydrogenated TiO_2 anatase/rutile phase heterojunction is fabricated and used for photoelectrochemical water splitting to generate clean H_2 energy under solar light. This TiO_2 phase heterojunction photocatalyst material with core-shell structures is accurately prepared by a hydrothermal method to grow the core of rutile TiO_2 nanorod arrays and an ALD technology to form the shell of the anatase TiO_2 layer with a controllable thickness, followed with a hydrogenated treatment to introduce some disordered structures and oxygen vacancies to the TiO_2 phase heterojunction. This new structured TiO_2 photocatalyst material yields a high photocurrent density of 3.88 mA cm^{-2} at 1.23 V$_{vs.RHE}$ under simulated solar light (100 mW cm^{-2}) with a maximum IPCE of 59.7% at the wavelength of 380 nm. These values are almost 3.8 and 7.4 times higher than that of the bare rutile TiO_2, respectively. The enhanced photoelectrochemical performances are mainly attributed to the synergistic effect of the core-shell phase heterojunction, highly ordered structure and post-hydrogenated treatment to accelarate the separation and transmission of the photogenerated electrons and holes. This hydrogenated TiO_2 core-shell phase heterojunction indicates promising potential applications in the fields of photoelectrocatalysis and photovoltaic devices under solar light.

1. Introduction

Recently, the energy crisis and environmental pollution have become two highly important factors restricting the development of modern society. As one clean energy, the hydrogen produced from water has attracted increasing attention since the discovery of photoelectrochemical (PEC) water splitting to generate clean hydrogen energy from solar light and water via photocatalyst [1,2]. For practical applications, the photocatalyst employed for water splitting should be stable and highly efficient. As one of the most studied photocatalysts, TiO_2 has attracted extensive attentions for water splitting and some other photovoltaic devices, owing to its low cost, easy to obtain, nontoxic, and high intrinsic catalytic activity under UV light [3–8]. However, the weak light absorption under solar light and the low hydrogen production efficiency usually greatly limit its further applications.

Generally, the light response property and photocatalytic activities of TiO_2 are highly dependent on its structure and composition, which are two key factors influencing the band gap, separation and

transmission of photoexcitations, as well as the photon-to-hydrogen energy conversion efficiency. Various methods have been studied to improve the PEC properties of photocatalyst, including metal or nonmetal doping, ordered structural design, compositing with narrow bandgap semiconductors, plasma treatment, and so on [9–17]. Among these strategies, fabrication of heterojunction structure was proven to be an efficient means to accelerate the separation and transmission of photogenerated charge carriers and inhibit the recombination of electron–hole pairs [18,19]. In previous works, different composite semiconductors, such as TiO_2/Cu_2O [20], TiO_2/CdS [21], and $TiO_2/SrTiO_3$ [22], were predominantly used to form heterojunctions to enhance the PEC properties of TiO_2 nanomaterials, owing to the quantum effect, larger mobility, and the singular properties of two dimensional space. For these heterojunctions with TiO_2 as the main photocatalyst material, the band position, stability, and the composite interface structure of the other matched material usually importantly influence the final photocatalytic activities of the newly formed heterojunctions. Therefore, heterojunctions with suitable matched band positions, good stability,

---

effective contact interface, and large heterojunction contact area are highly required. Meanwhile, anatase (E = 3.2 eV) and rutile (E = 3.0 eV) TiO_2 can also form the phase heterojunction [23–28]. Given the specific band structure and high built-in potential, photogenerated electrons and holes can migrate in opposite directions on the surface between anatase and rutile phase. This process can help reduce the recombination rate of photogenerated charge carriers and improve the PEC water-splitting properties [29–34]. While most of the previous anatase/rutile phase heterojunctions were based on powder materials and disordered structures, and it is difficult to synthesize them in a controllable manner [35,36]. In this case, the disordered phase heterojunctions could also serve as the positions for the recombination of electron-hole pairs. Thus, fabricating the ordered TiO_2 phase heterojunction with core-shell anatase/rutile structures is a new route for facilitating the charges separation. However, it is still a challenge to synthesize the ordered TiO_2 phase heterojunction in a controllable manner.

Herein, we demonstrate a new method to fabricate TiO_2 anatase/rutile phase heterojunction with core-shell structure by combining atomic layer deposition (ALD) technology and in situ chemical growth strategy. To narrow the band gap and improve the photoelectrocatalytic activities of the TiO_2 phase heterojunction, we adopted hydrogenation treatment to synthesize a hydrogenated anatase and hydrogenated rutile phase heterojunction (referred to H-B-A/R TiO_2 NRs), which can further enlarge the solar light absorption by introducing a disordered structure and oxygen vacancies [9,37–42]. The 3D branched structure of TiO_2 NRs can be controlled by adjusting the hydrothermal and chemical growth condition, and the rate of the anatase/rutile core-shell phase heterojunction can be controlled by adjusting the deposition cycles of anatase TiO_2 by ALD. These in situ growth methods enabled the anatase TiO_2 layer to conform and uniformly covered the branched rutile TiO_2 NRs to form the A/R phase heterojunction with a tight and ordered interface. Such hydrogenated TiO_2 NRs with 3D branched structures showed high photoharvesting abilities under solar light. Moreover, the core-shell phase heterostructure could also facilitate the charges separation and dramatically enhance the water-splitting efficiency.

2. Experimental section

2.1. Preparation of rutile TiO_2 NRs

Single-crystal rutile TiO_2 NRs were fabricated on a fluorine-doped tin oxide (FTO) glass slide by a modified hydrothermal method [5]. In a typical preparation procedure, 30 mL deionized water was mixed with 30 mL of concentrated hydrochloric acid (38% by weight) in a Teflon-lined stainless steel autoclave (100 mL volume). The mixture was then stirred for 5 min before 0.72 mL of titanium butoxide (98%, Aldrich) was added. After stirring for another 5 min, a piece of FTO (1 × 6 cm^2) glass ultrasonically cleaned with acetone, isopropanol, ethanol, and deionized water in sequence for a certain time was placed at a 30° angle against the wall of the Teflon-liner with the conducting side facing down. The hydrothermal synthesis was conducted at 170 °C for 6 h. After the autoclave was naturally cooled to room temperature, the samples were washed with distilled water several times until the pH became 7 to obtain well-aligned rutile TiO_2 NRs.

2.2. Preparation of branched rutile TiO_2 NRs

An in situ chemical growth method was used to prepare rutile TiO_2 NRs with 3D
branched structures. The as-obtained rutile TiO_2 NRs with smooth surfaces were horizontally immersed into a mixed aqueous solution consisting of 100 mL deionized water, 0.4 mL concentrated hydrochloric acid (38% by weight), and 0.09 mL $TiCl_4$ solution. The NRs were then maintained at 50 °C for 8 h in a thermostat water bath. The

obtained sample was thoroughly washed with distilled deionized water and subsequently dried in a vacuum oven at 80 °C for 10 h.

2.3. Preparation of branched rutile/anatase TiO_2 NRs with core-shell phase heterojunction structure

The obtained branched rutile TiO_2 NRs were introduced into an ALD chamber for depositing another TiO_2 layer (shell) uniformly on the surface of rutile TiO_2 NRs and the branches (core) with titanium isopropoxide (TIPT) and deionized water as precursors. The deposition temperature was 150 °C. One ALD cycle process of TiO_2 deposition consisted of a 1 s pulse of TIPT, 8 s exposure to TIPT, 20 s purge with nitrogen followed by a 0.1 s pulse of H_2O, 8 s exposure to H_2O and eventually 25 s purge with nitrogen. After depositing for 30–150 cycles, the branched rutile TiO_2 NRs with a thin amorphous TiO_2 layer were placed into a furnace at 450 °C for 2 h in air to transform the outside TiO_2 layer from the amorphous phase to anatase. Eventually, the branched rutile/anatase TiO_2 NRs with core-shell phase heterojunction structure were fabricated completely.

2.4. Preparation of hydrogenated branched TiO_2 NRs with core-shell rutile/anatase phase heterojunction structure

Finally, the as-prepared branched rutile/anatase TiO_2 NRs with core-shell phase
heterojunction structure were calcined again in a quartz tube furnace under hydrogen atmosphere at 400 °C for 2 h with a heating rate of 5 °C min^{-1} and a hydrogen flow rate of 30 mL min^{-1}. This process resulted in the production of branched TiO_2 NRs with hydrogenated core-shell anatase/rutile phase heterojunction structures.

2.5. Material characterization

The morphologies of the samples were characterized by scanning electron microscopy (SEM; JSM-6701 F, JEOL Inc., Japan). Transmission electron microscopy (TEM) images were then obtained from a FEI Tecnai G2 TF20 transmission electron microscope with a field-emission gun operating at 200 kV. X-ray diffraction (XRD) analysis (Bruker D8 ADVANCE) and UV–vis light (UV–vis) diffusion reflectance spectroscopy (U-4100) were carried out. X-ray photoelectron spectroscopy (XPS) was performed under a ultra-high vacuum (< 10^{-6} Pa) with a pass energy of 93.90 eV on an ESCALAB 250Xi system equipped with a dual X-ray source by using an Mg anode and a hemispherical energy analyzer. All the energies were calibrated with contaminant carbon (C1 s = 284.6 eV) as reference. Photoluminescence (PL) spectroscopy was obtained by a high-resolution spectrofluorometer (UK, Edinburgh. Instruments, FLS980) equipped with a 500 W xenon lamp as an excitation source.

2.6. Photoelectrocatalytic characterization

The PEC properties of the samples were evaluated in a PEC cell with a rounded quartz window for light illumination. The cell included a three-electrode system with the samples as the working electrode, a platinum plate as counter electrodes, and a saturated calomel electrode (SCE) as the reference electrode in 0.1 M NaOH solution. The photoanodes with an effective irradiation area of 1 cm^2 were illuminated with a 300 W Xe lamp coupled with an AM 1.5 G filter (PLS-SXE300UV, Beijing Perfectlight Technology Co., Ltd.) calibrated to 100 mW cm^{-2} by a radiometer (CEL-NP2000, Beijing Au-light Co., Ltd.). The measured potential versus the SCE reference electrode was converted to the reversible hydrogen electrode (RHE) by the Nernst Eq. (1)

$$E_{RHE} = E_{SCE} + E_{SCE}^{\theta} + 0.059pH \tag{1}$$

where E_{RHE} is the converted potential versus RHE, E_{SCE} is the

experimental potential measured against the SCE, E_{SCE}^{θ} is the standard potential of the SCE at 25 °C (0.2412 V), and pH is the electrolyte pH. Linear sweep voltammetry curves and amperometric I–t curves were obtained with a CHI660E electrochemical workstation (CH Instruments Co., Shanghai, China) at the scan rate of 10 mV s^{-1}. The incident-photon-to-current conversion efficiency (IPCE) values were measured by using a 150 W Xe lamp (SM-25 Hyper Monolight, Japan). The light intensity of the moonlight was calibrated with a standard silicon photodiode. The IPCE values were obtained by using the following Eq. (2) [43]

$$IPCE(\%) = \frac{1240 \times j_{ph}}{\lambda \times I} \qquad (2)$$

where j_{ph} is the steady-state photocurrent density at a specific wavelength, λ is the wavelength of the incident light, and I is the light intensity for the selected wavelength λ at the film surface. The evolution of hydrogen and oxygen by photoelectrochemical water splitting was conducted in an air-tight reactor connected to a closed gas circulation system. The hydrogenated 3D anatase/rutile phase heterojunction TiO$_2$ NR photoanodes were biased at 1.23 V$_{vs.RHE}$ in a stirred aqueous solution of 0.1 M NaOH under AM 1.5 G simulated sunlight. The amount of hydrogen or oxygen was determined by gas chromatography (GC-7920).

3. Results and discussion

Fig. 1 shows a typical fabrication route of H-B-A/R TiO$_2$ NR photoanodes combining in situ chemical growth method and ALD technology. First, the rutile TiO$_2$ NR arrays of single crystal were grown vertically on the FTO glass substrate via a modified hydrothermal method with a dip angle of 30° against the Teflon-liner wall. Second, the specific surface area of the rutile TiO$_2$ NRs for absorbing photolight was enhanced. This result was achieved by the in situ chemical growth of branched TiO$_2$ NRs with some smaller rutile NRs on the surface of the TiO$_2$ NRs trunk. The method was conducted by immersing the rutile TiO$_2$ NR arrays into TiCl$_4$ solution at 50 °C for 8 h. Third, the anatase/

rutile phase heterostructure was formed by employing the ALD technique to deposit a uniform anatase TiO$_2$ layer on the surface of the branched rutile TiO$_2$ NRs. Fourth, the absorption under solar light was enhanced by hydrogenating the branched anatase/rutile TiO$_2$ NRs in a hydrogen and argon atmosphere to obtain the final hydrogenated anatase/rutile TiO$_2$ phase heterojunction (H-B-A/R TiO$_2$ NRs).

Fig. 2 shows the top views and cross-sectional views of the rutile TiO$_2$ NRs after hydrothermal synthesis, the branched rutile TiO$_2$ NRs after in situ chemical growth, the anatase/rutile phase heterostructure of branched TiO$_2$ NRs, and the anatase/rutile phase heterostructure of the branched TiO$_2$ NRs after hydrogenation treatment. In Fig. 2a, cubic-column-like TiO$_2$ NRs with smooth surfaces were vertically aligned on the FTO substrate surface with a diameter of 50–100 nm and length of about 2 μm. After the immersion process, some needlelike branches symmetrically grew on the surface of the TiO$_2$ NRs with an average diameter of 20 nm and length of about 70–80 nm. Interestingly, these branched TiO$_2$ NRs with 3D structures remained straight without agglomeration after the in situ chemical growth process (Fig. 2b). Fig. 2c reveals the morphologies of the branched TiO$_2$ NRs after overcoating a thin TiO$_2$ layer by ALD for 70 deposition cycles, followed by calcination at 450 °C for 2 h in air to convert the amorphous ALD deposition layer to anatase. Compared with the morphology of the branched TiO$_2$ NR, the size of the TiO$_2$ NR trunk and the needlelike branches obviously increased, with the branch diameters enlarging from about 20 nm to about 30 nm. This result matched well with the deposition thickness achieved by ALD for 70 cycles. More information about the TEM images of the bare rutile TiO$_2$ NRs, the branched rutile TiO$_2$ NRs and the anatase/rutile phase heterostructure of branched TiO$_2$ NRs are shown in supporting information of Fig. S1. As shown in Fig. 2d, the trunk and branch morphologies of the H-A/R TiO$_2$ NRs were not obviously altered after the hydrogenation process. This finding suggests that the hydrogenation treatment could not change the overall morphologies of the branched TiO$_2$ NRs at the micrometer scale.

The microstructure and the interfaces of the anatase/rutile phase heterojunctions of TiO$_2$ NRs were further characterized by high-resolution TEM (HRTEM), as shown in Fig. 3. Meanwhile, Fig. 3a and b
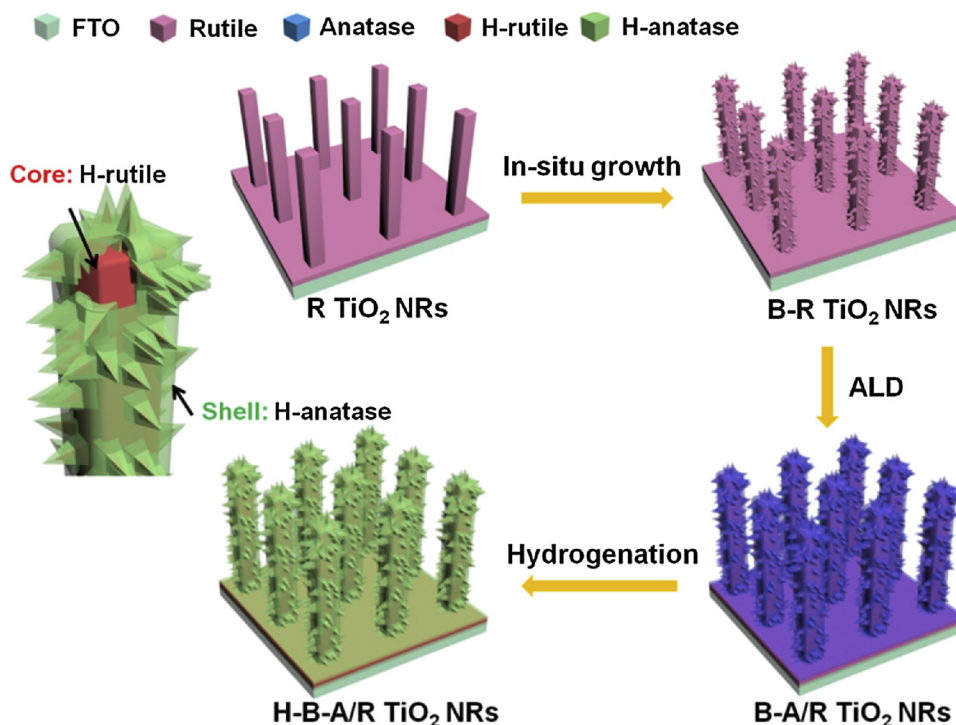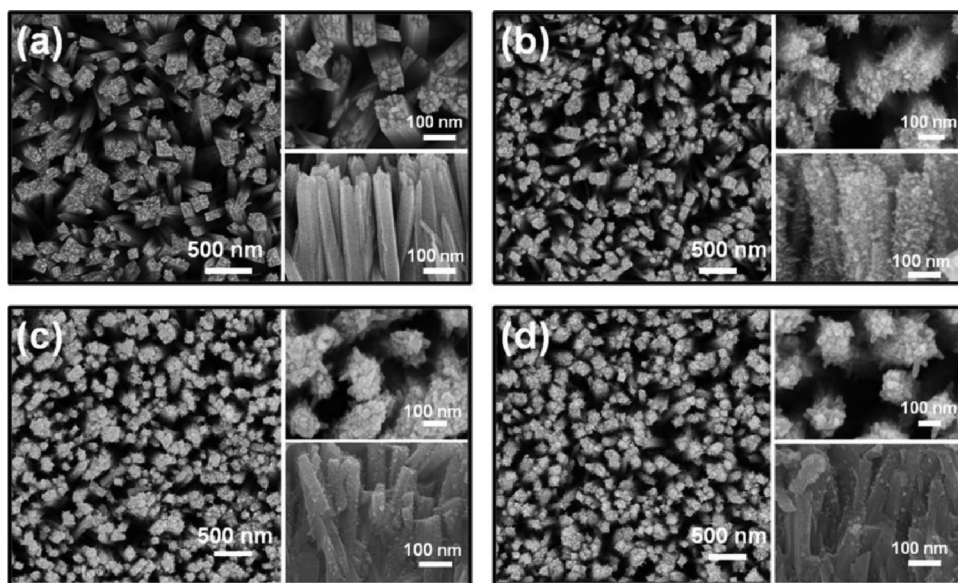

Fig. 1. Schematic of the preparation processes of hydrogenated and branched TiO$_2$ NRs with a core-shell rutile/anatase phase heterojunction structure (H-B-A/R TiO$_2$ NRs).
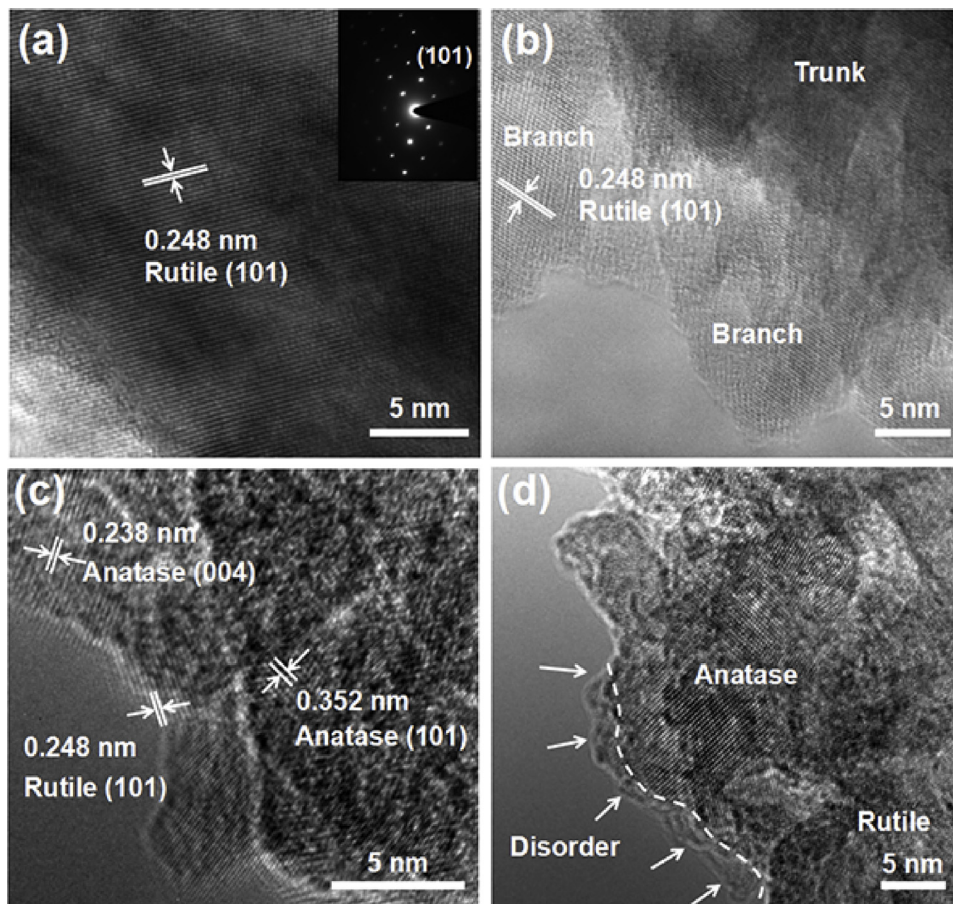
Fig. 2. Field-emission SEM images of (a) rutile TiO$_2$ NRs, (b) branched rutile TiO$_2$ NRs, (c) the anatase/rutile phase heterostructure of branched TiO$_2$ NRs, and (d) the anatase/rutile phase heterostructure of branched TiO$_2$ NRs after hydrogenation. The insets show the high-magnification images of the top views and cross-sectional views, respectively.

display the HRTEM images of single-crystal TiO$_2$ NRs and the branched TiO$_2$ NRs after in situ chemical growth, respectively. The crystalline phases of these structures were all attributed to the (101) lattice crystal plane of rutile phase. Fig. 3a inset presents the selected-area electron diffraction pattern, which can further confirm that the TiO$_2$ NRs are single crystalline. In particular, for the branched TiO$_2$ NRs, the TiO$_2$ NR trunk and the needlelike branches are all rutile. This result indicates that only the rutile TiO$_2$ nanocrystalline formed during the in situ chemical growth process. The rutile nanocrystalline provides the

skeleton frame for the synthesis of the layered anatase/rutile phase heterojunction. After the deposition of amorphous TiO$_2$ by ALD and the following crystallization treatment at 450 °C for 2 h, a thin anatase TiO$_2$ layer of about 5 nm thickness was uniformly formed on the surface of the branched rutile TiO$_2$ NRs (Fig. 3c). HRTEM directly confirmed that the (101) and (004) lattice crystal planes of anatase TiO$_2$ grew in the conjunction with rutile TiO$_2$ on the TiO$_2$ NR trunk and branch surfaces. The fringe spacing of 0.248 nm exactly corresponded to the (101) lattice crystal plane of the rutile phase. Thus, the core-shell phase

Fig. 3. HRTEM images of (a) rutile TiO$_2$ NRs, (b) branched rutile TiO$_2$ NRs, (c) anatase/rutile phase heterostructure of branched TiO$_2$ NRs, and (d) the anatase/rutile phase heterostructure of branched TiO$_2$ NRs after hydrogenation. The figures display the anatase and rutile phase heterojunction interface and the disordered layer after hydrogenation treatment. The inset in (a) is the selected-area electron diffraction pattern.
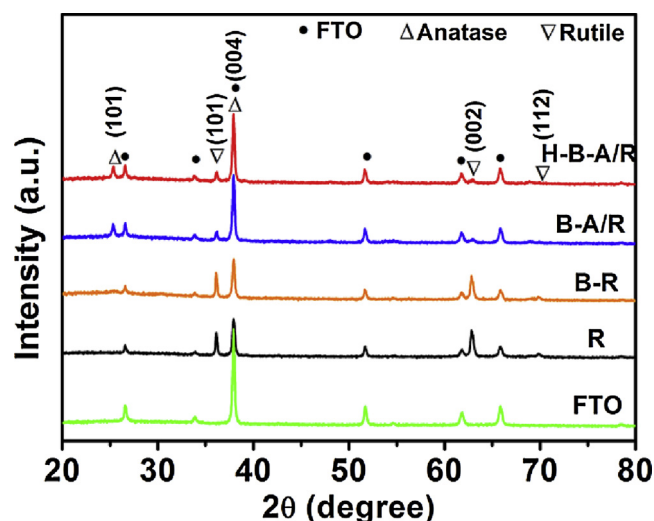
Fig. 4. XRD patterns of rutile TiO_2 NRs, the branched rutile TiO_2 NRs, anatase/rutile phase heterostructure of branched TiO_2 NRs, the hydrogenated anatase/rutile phase heterostructure of branched TiO_2 NRs, and the FTO glass slide.

heterojunction, with the branched rutile TiO_2 NRs as the core and the external covering anatase TiO_2 layer as the shell, was formed. Fig. 3d reveals the HRTEM images of the anatase/rutile phase heterostructure of the branched TiO_2 NRs after hydrogenation treatment. In the figures, the interfaces of the anatase/rutile phase heterostructure and the distinct disordered layer are clearly shown. The figures indicate the successful synthesis of the hydrogenated anatase and hydrogenated rutile phase heterojunction.

The phase and crystal structure of the as-prepared samples were further analyzed by XRD (Fig. 4). The pattern curve at the bottom is the characteristic peak of FTO substrate (JCPDS No. 41-1445), which is used as the reference (Fig. 4). In the other four patterns, the peaks all refer to the TiO_2 phase, except for the FTO substrate. Notably, the typical diffraction peaks (101) and (002) of the single-crystal rutile TiO_2 phase are obviously observed at 36.085° and 62.740° in the samples of the as-prepared TiO_2 NRs after hydrothermal treatment and the branched TiO_2 NRs after in situ chemical growth and post-heat treatment at 450 °C for 2 h (JCPDS No. 21-1276). This result indicates that the newly formed TiO_2 branches were also only rutile crystal. The findings also matched well with the interplanar lattice spacing of 0.248 nm, which was attributed to the rutile TiO_2 NRs (101) (Fig. 2b). After the subsequent ALD growth of the amorphous TiO_2 layer and the post-heat treatment at 450 °C for 2 h to complete the crystallization, a new and typical anatase diff ;raction peak appeared at 25.2° (JCPDS No. 21-1272). This peak corresponded to the successful synthesis of the anatase/rutile phase heterostructure based on the branched rutile TiO_2 NRs. Moreover, compared with the result of the branched rutile TiO_2 NRs, the peak intensity of the anatase/rutile TiO_2 NRs near 37.8° was also enhanced. This finding was attributed to the overlap of the diff ;raction peak of the FTO substrate centered at 37.9° with that of the newly formed anatase phase (004). Lastly, no difference in patterns of the anatase/rutile phase heterostructure of the branched TiO_2 NRs was noted before and after hydrogenation treatment. Hence, the hydrogenation treatment at 400 °C only slightly influenced the crystallization.
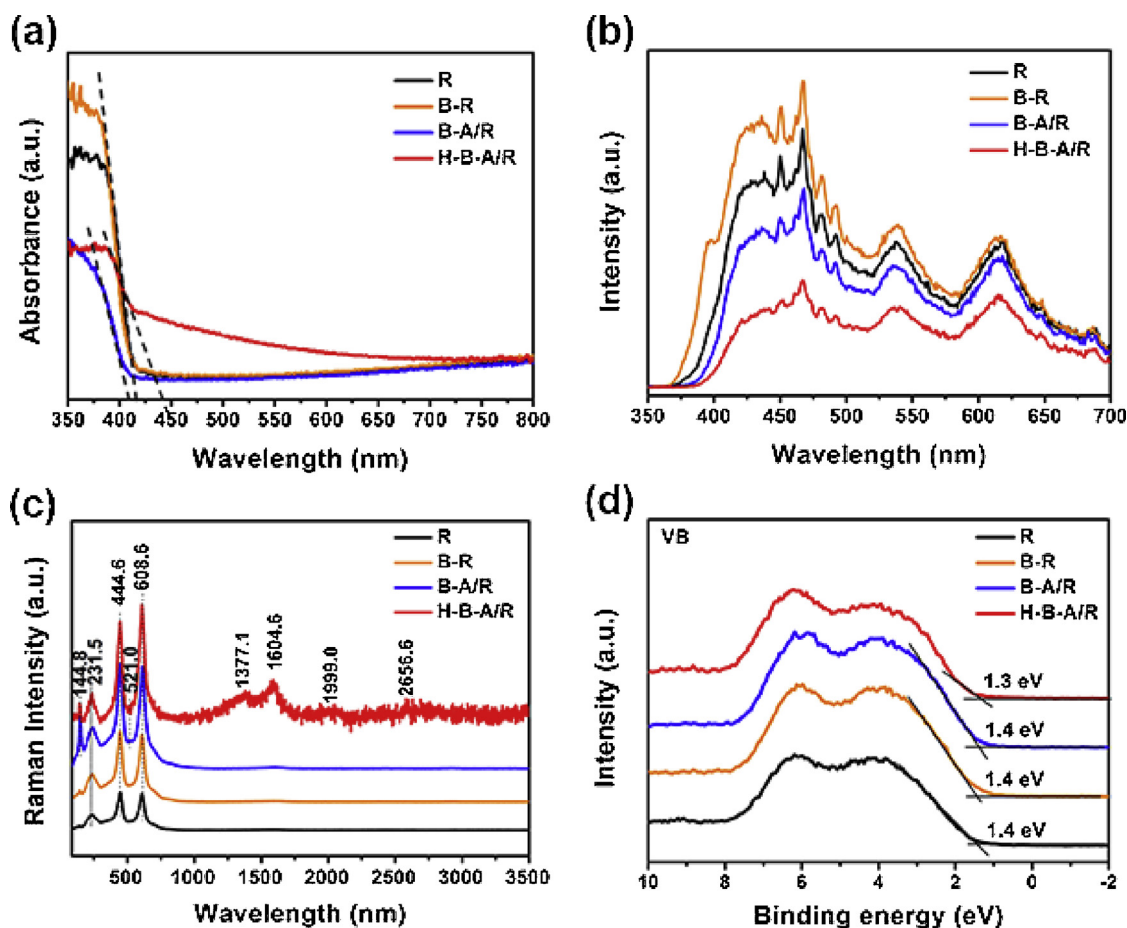
Fig. 5a shows the UV–vis absorption spectra of the as-obtained samples. The absorption edges of the rutile TiO_2 NRs and branched rutile TiO_2 NRs were all located at approximately 413.6 nm. This location agreed with the estimated 3.0 eV band gap energy of the rutile TiO_2 sample. It also indicates that the branched TiO_2 nanomaterials were of rutile phase under the in situ chemical growth method. After the deposition of the anatase layer on the branched rutile TiO_2 NRs to fabricate the phase heterojunction, the anatase/rutile phase heterojunction TiO_2 NRs displayed a small blue shift. The absorption edge of

phase heterojunction is determined to be 408.8 nm, which is lower than that of rutile TiO_2 NRs and branched rutile TiO_2 NRs. This shift is due to the successful formation of the anatase TiO_2 with a strong absorption in the UV light region through ALD technology and post heat-treatment [44–47]. The hydrogenated phase heterojunction TiO_2 NRs presented obvious red shifts in band gap transition and enhanced absorption in the visible-light region. The absorption edge of the hydrogenated phase heterojunction TiO_2 NRs is determined to be 441.3 nm. From the above, the band gap energy of as-obtained samples are evaluated to be approximately 3.00 eV, 3.00 eV, 3.03 eV and 2.81 eV. Therefore, after hydrogenated treatment, the band gap was narrowed about 0.19 eV, 0.21 eV and 0.22 eV, respectively. In addition, hydrogenated phase heterojunction TiO_2 NRs shows enhanced absorption in the visible-light region from 450 nm to 750 nm. These effects were achieved because oxygen vacancy formed as the mid-gap energy levels and the disordered structures narrowed the band gap after the hydrogenation process [9,38,48–50].

According to previous reports [51], the PL emission spectrum was certified to be a useful approach for evaluating the extent of transfer and separation, as well as the trapping of charge carriers, within the anatase and rutile phases of TiO_2 nanomaterials. The transfer behavior of the photogenerated electron and hole pairs can be investigated as the recombination of the free charges contribute dramatically to the emission signals of the PL spectra [52]. Fig. 5b presents the PL spectra of the as-obtained photoanodes measured under 200 nm excitation. The pure rutile TiO_2 NRs (referred to as R) and the branched rutile TiO_2 NRs (referred to as B-R) showed a broad PL band in the 350–500 nm region. The intensity of the bands were higher than those of others. This discrepancy may be derived from of the radiative recombination of the self-trapped exciton caused by the existence of probable defect sites and surface states. The PL intensity of the branched rutile TiO_2 NRs was slightly stronger than that of pure TiO_2 NRs. This difference may be due to increased density of defect sites that was caused by the enhanced surface areas. Even so, the branched rutile TiO_2 NRs with enhanced surface areas can absorb additional light and show improved PEC properties. Meanwhile, the branched rutile TiO_2 NRs were precisely coated with anatase phase by ALD to form the core-shell anatase/rutile phase heterostructures (referred to B-A/R). However, the PL signal instantly weakened in the core-shell anatase/rutile phase heterostructures branched TiO_2 NRs. This effect reveals that the specific band structure of the two TiO_2 crystalline phase can promote the migration of charge carriers between the anatase and rutile phases and consequently depress charge-carrier recombination. After hydrogenation treatment, the PL signal sharply decreased because of the appearance of oxygen vacancy as the mid-gap energy levels in the hydrogenated anatase/rutile TiO_2 NRs, which could significantly improve the separation and transfer efficiency of photogenerated electron and hole pairs.

Raman spectra were used to further examine the structural changes of the anatase/ rutile phase heterojunction TiO_2 NRs after hydrogenation treatment. Three Raman-active modes with frequencies at 231.5, 444.6, and 608.6 cm^{-1} for the above four photoanodes, respectively, were are all attributed to the rutile phase (Fig. 5c). The Raman spectra of the pure rutile TiO_2 NRs and branched rutile TiO_2 NRs only consisted of characteristic peaks of the rutile phase, whereas the core-shell anatase/rutile phase heterostructure branched TiO_2 NRs produced a typical anatase Raman band at 144.8 and 521 cm^{-1}. After hydrogenation treatment, new peaks appeared at 1377.1, 1604.6, 1999.0, and 2656.6 cm^{-1} appeared for the hydrogenated core-shell anatase/rutile phase heterostructure TiO_2 NRs. These Raman bands could not be assigned to any of the three polymorphs of TiO_2, which indicates that structural changes occur after hydrogenation, resulting in disorders that can activate zone-edge and otherwise Raman-forbidden modes by breaking down the Raman selection rule [9]. It can be also proved by the HRTEM images, which was shown in Fig. 3d. The distinct disordered layer are clearly appeared on the surface of phase heterostructure after hydrogenated treatment. Large amounts of lattice
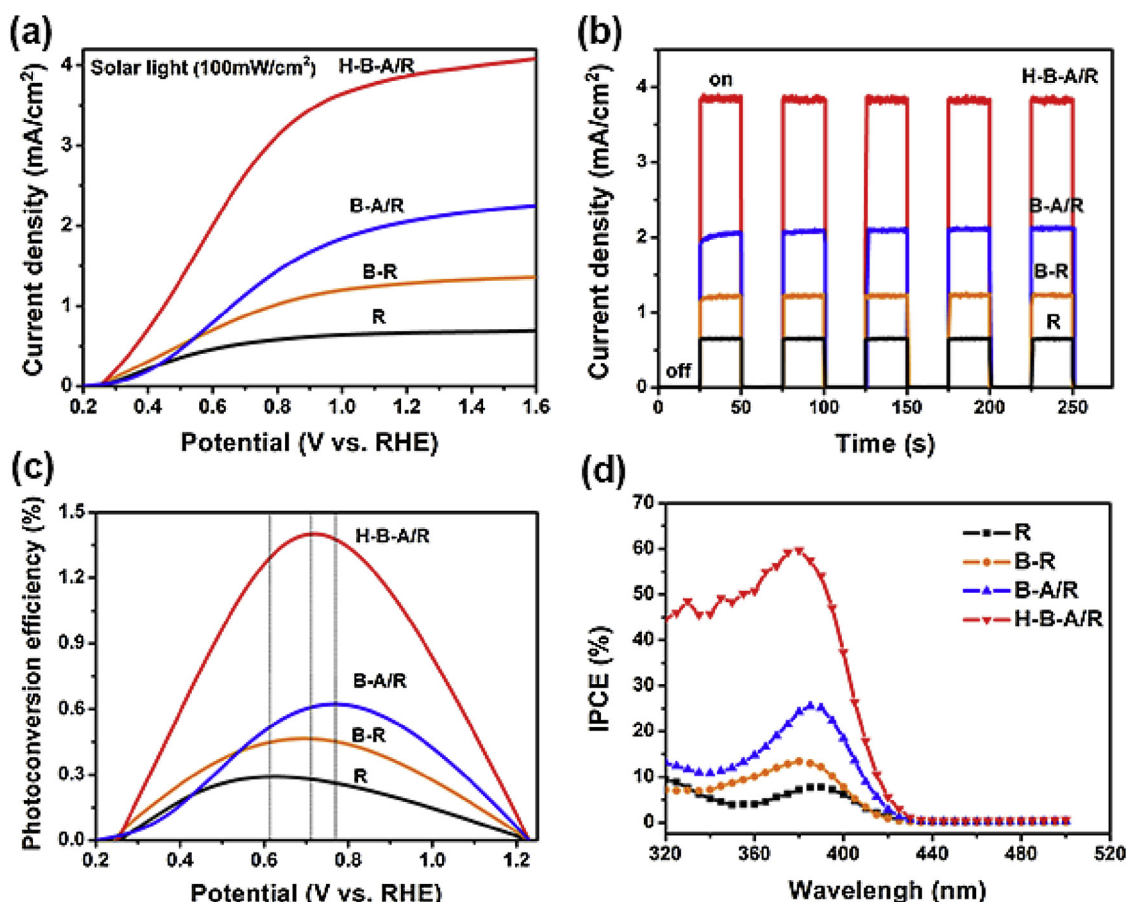
Fig. 5. (a) UV–vis absorption spectra, (b) PL spectra, (c) Raman spectra, and (d) XPS VB spectra of the rutile TiO₂ NRs, branched rutile TiO₂ NRs, anatase/rutile phase heterostructure of branched TiO₂ NRs, and the hydrogenated anatase/rutile phase heterostructure of the branched TiO₂ NRs.

disorder in semiconductors could yield mid-gap states whose energy distributions differ from that of a single defect in a crystal [9,53]. Fig. 5d shows the valence band (VB) XPS spectra of the as-obtained photoanodes. In a report by Chen and coworkers [9], white TiO₂ nanocrystals displayed the typical VB density-of-states characteristics of TiO₂, with the edge of the maximum energy at about 1.26 eV. In our work, the unhydrogenated photoanode was observed with a VB edge of about 1.4 eV below the Fermi energy for all samples. After the hydrogenation treatment, the hydrogenated core-shell anatase/rutile phase heterostructure branched TiO₂ NRs exhibited small VB blue-shifts by 0.1 eV because of the introduction of band tail states and surface disorder.

We carried out XPS to further demonstrate the change in surface chemical bonding of the as-obtained TiO₂ photoanodes and the effect on enhanced PEC properties induced by hydrogenation treatment. In Fig. S2, the Ti 2p XPS spectra were almost identical for all the photoanodes, with Ti 2p3/2 and 2p1/2 peaks centered at the binding energies of 458.88 and 464.48 eV, which are consistent with the typical values for TiO₂ [54,55]. The Ti $2p_{3/2}$ XPS spectrum of the hydrogenated anatase/rutile TiO₂ NRs can be separated to two peaks at 458.9 eV and 458.2 eV, which can be ascribed to Ti⁴⁺ and Ti³⁺ species (as shown in Fig. S3) [48]. Due to the reducing action of hydrogen gas (H₂), by heating TiO₂ nanomaterials in a hydrogen atmosphere, plenty of oxygen vacancies, associated with Ti³⁺ were introduced in hydrogenated anatase/rutile TiO₂ NRs [52]. Many of studies have also confirmed that oxygen vacancies (Ti³⁺ species) were induced by hydrogenation in TiO₂ [9,41,56,57]. As a result, the bandgap narrowing is dictated by the synergistic presence of oxygen vacancies and disorder structure on the surface [41]. As shown in Fig. S4, the O 1s XPS spectra

of H-B-A/R showed dramatic differences among the four spectra after hydrogenation treatment. A single peak centered at 529.98 eV and a broader shoulder at higher binding energy were noted. This result can be fitted into three peaks at about 529.98 and 531.58 eV, which were attributed to O−Ti (O$_{Ti}$) and Ti−OH (O$_{OH}$). The Ti−OH peak was expected for the hydroxyl group on a TiO₂ surface, which has been reported to be located at about 1.5–1.8 eV higher binding energy corresponding to the O 1s of TiO₂ [58]. For the H-B-A/R, compared with the untreated samples, the atom percentages of Ti–OH increased to 30.62%. The results indicate that H₂ reacted with TiO₂ and produced additional hydroxyl groups on the surface of the TiO₂ NRs [59].

To further study the PEC performances of the samples, we used a standard three-electrode electrochemical cell with Pt foil as counter electrode, SCE as reference electrode, and TiO₂-NR-based photoelectrodes as working electrode for PEC measurements in 0.1 M NaOH aqueous solution under simulated solar light at 100 mW cm⁻². Fig. 6a shows the linear sweep voltammograms of rutile TiO₂ NRs, branched rutile TiO₂ NRs, anatase/rutile TiO₂ NRs, and hydrogenated anatase/rutile TiO₂ NRs under simulated solar light at a scan rate of 10 mV s⁻¹. The photocurrent density of the smooth rutile TiO₂ NRs were merely 0.67 mA cm⁻² at 1.23 V$_{vs.RHE}$ under simulated solar light (100 mW cm⁻²) because of the low light absorption efficiency and high recombination rate of the photogenerated electron–hole pairs on the TiO₂ NRs. After the smooth TiO₂ NRs were dipped into TiCl₄ solution for 8 h at 50 °C to form the branched rutile TiO₂ NRs, the photocurrent density was increased to 1.29 mA cm⁻² at 1.23 V$_{vs.RHE}$ under simulated solar light. This effect was mainly attributed to the large surface area of the branched TiO₂ NRs for the improved light absorption and enhanced interfacial charge transfer. Furthermore, after the formation of the core-

Fig. 6. PEC properties of the rutile TiO_2 NRs, branched rutile TiO_2 NRs, anatase/rutile phase heterostructure of branched TiO_2 NRs, and the hydrogenated anatase/rutile phase heterostructure of branched TiO_2 NRs. (a) Linear sweep voltammograms under simulated solar light (100 mW cm^{-2}), (b) the photocurrent responses (light on and light off) at the potential of 1.23 $V_{vs.RHE}$, (c) the calculated photoconversion efficiency, and the (d) IPCE spectra of the samples collected at the incident wavelength range from 320 nm to 500 nm at a potential of 1.23 $V_{vs.RHE}$ in 0.1 M NaOH.

shell phase heterojunction by ALD, the photocurrent density of the anatase/rutile TiO_2 NRs reached the high value of 2.08 mA cm^{-2} at 1.23 $V_{vs.RHE}$. This value was about 3.1 and 1.6 times that of the rutile TiO_2 NRs and branched TiO_2 NRs electrodes, respectively. The anatase/rutile phase heterojuncture is clearly beneficial in enhancing the PEC properties because of the unique band structures of the anatase and rutile form a high built-in potential in the phase heterojunction. This high potential permits the photogenerated electrons to transfer from the anatase phase into the rutile phase. Meanwhile, the photogenerated holes transfer from the rutile phase into anatase phase. The above-mentioned processes then result in photogenerated electrons and holes migrating in opposite directions [23,25]. This effect can also suppress the recombination of photogenerated electron and hole pairs.

When the anatase/rutile TiO_2 NR photoelectrode was again heat treated in a quartz tube furnace under hydrogen (30 sccm) and argon (70 sccm) atmosphere at 400 °C for 2 h, the photocurrent density of the hydrogenated anatase/rutile TiO_2 NRs reached 3.88 mA cm^{-2} at 1.23 $V_{vs.RHE}$ under simulated solar light (100 mW cm^{-2}). This value was almost 4.8 times higher than that of the bare rutile TiO_2 NR photoanode. The strong solar light absorption accounted for the disordered layer as the mid-gap energy levels, which were generated because of the strong reductive ability of hydrogen gas during the hydrogenation process. The lower-energy mid-gap energy levels operating as the shallow donor states between the conduction band (CB) and VB prevent the fast recombination of photoexcited charge carriers. Introducing oxygen vacancy can also help improve electronic conductivity [9,53]. Moreover, the synergy of the unique band structure of the anatase/rutile phase heterojuncture, the disordered layer on the samples, and

the oxygen vacancy after hydrogenated treatment can cause the TiO_2 NR photoanode with core-shell branched phase heterostructures to acquire a dramatically enhanced photocurrent density under simulated solar light. As shown in Fig. S5, the hydrogenated phase heterojuncture TiO_2 NRs also possess the superior PEC performance comparing with the commercial P25 (TiO_2).

Fig. 6b shows the instantaneous photocurrent responses of the above samples under the simulated solar light (100 mW cm^{-2}) at the potential of 1.23 $V_{vs.RHE}$ with and without a light baffle. All the photoelectrodes released no photocurrent in the dark, but the photoanodes expressed a remarkable photocurrent density and reached a steady value quickly as light was applied. The sharp increase and decrease of photocurrent density with the on/off switch were closely related to the quick photoresponse and good stability for all the samples. Fig. 6c shows the photoanodes' photoconversion efficiency, which were calculated by the Eq. (3) [48]

$$\eta = I(1.23 - V)/J_{light} \tag{3}$$

where I is the photocurrent density at the measured bias, V is the applied bias versus RHE, and J_{light} is the irradiance intensity of 100 mW cm^{-2}. The photoconversion efficiency of the hydrogenated A/R TiO_2 NRs with branched structure reached 1.4% at 0.71$V_{vs.RHE}$; this value was almost 3.8 times that of the pure TiO_2 NRs (0.29% at 0.71 $V_{vs.RHE}$) (Fig. 6c). The high photoconversion efficiency was chiefly derived from the synergistic effect of the oxygen vacancy, branched and ordered structure, and anatase/rutile phase heterojunction. The branched A/R TiO_2 NRs and branched rutile TiO_2 NRs also exhibited the enhanced photoconversion efficiency of 0.62% and 0.46% at 0.71 $V_{vs.RHE}$. To

display the PEC properties of the as-prepared electrodes with a standard form, we determined the IPCE under a monochromatic light irradiation at 1.23 $V_{vs.RHE}$ (Fig. 6d). This measure is another important parameter for characterizing the photoconversion efficiency of different photoanodes because of the parameter's independence from the light sources and filters used in the measurements [21]. Compared with the rutile TiO_2 NRs and branched rutile TiO_2 NRs, the TiO_2 NR electrodes with phase heterojunction structures exhibited significantly enhanced photoactivity over the entire UV region. This behavior further proved that the anatase/rutile phase heterojunction with unique band structure and high built-in potential efficiently reduced the recombination rate of the photogenerated charge carriers and accelerated the transfer of electrons and holes under UV light. In particular, the IPCE values of the hydrogenated TiO_2 NR phase heterostructure were about 44% in the incident light wavelength range from 320 nm to 390 nm and reached a maximum value of 59.7% at a wavelength of 380 nm, which was 7.4 times that of pure rutile TiO_2 NRs. Moreover, Tables S1 and S2 compare the performance of some photocatalyst and heterojuncture in different systems. These results indicate that the hydrogenated phase heterostructure photoanodes achieved an increased separation rate of photoexcited electrons and holes for efficient PEC water splitting. Furthermore, at the wavelength range from 400 nm to 430 nm, the IPCE values for the hydrogenated TiO_2 NR phase heterostructure photoanodes were also higher than that of the unhydrogenated photoelectrodes. The photoresponse in the visible-light region primarily resulted from the introduction of a disordered layer and oxygen vacancy by hydrogenation treatment.

In addition, the thickness of the anatase TiO_2 layer significantly influenced the photocatalytic activities of the core-shell phase heterojunction material. Fig. 7a presents the relationship between the photocurrent density and the ALD cycles from 10 to 150 times (TiO_2 deposition thickness was about 0.07 nm per cycle). The branched TiO_2 NRs with 70 ALD cycles achieved the highest photocurrent density and indicated that the PEC properties of the phase heterostructure can be optimized by adjusting the rates of the anatase and rutile phases. To further verify the influence of anatase/rutile phase heterojuncture on the PEC properties for water splitting, we coated smooth rutile TiO_2 NRs with the anatase phase of 70 ALD cycles. After the formation of the core-shell phase heterojunction on smooth rutile TiO_2 NRs (referred to as A/R), the photocurrent density of A/R significantly improved (Fig. 7b) to about 1.44 times that of the pure rutile TiO_2 NRs (referred to as R). Thus, a phase heterojunction can lead to a much improved performance of rutile TiO_2 NRs. The core-shell phase heterojunction rutile TiO_2 NRs and smooth rutile TiO_2 NRs were also hydrogenated under hydrogen (30 sccm) and argon (70 sccm) atmosphere at 400 °C for 2 h, respectively. The photocurrent density of the hydrogenated core-shell phase heterojunction rutile TiO_2 NRs reached a high value of 3.46 mA cm^{-2} (Fig. 7c). However, the photocurrent density of hydrogenated rutile TiO_2 NRs was only 2.05 mA cm^{-2} at 1.23 $V_{vs.RHE}$ under simulated solar light (100 mW cm^{-2}). Moreover, the hydrogenated branched rutile TiO_2 NRs with and without anatase phase were studied. In Fig. 6c, the photocurrent density of the hydrogenated branched core-shell phase heterojunction rutile TiO_2 NRs (referred to as H-B-A/R) is higher than that of hydrogenated branched rutile TiO_2 NRs (referred to as H- B-R). All the results indicate that the anatase/rutile phase heterojuncture can improve the PEC properties for all the samples.

Fig. 8a presents the photocurrent–time curves of pure rutile TiO_2 NRs, branched rutile TiO_2 NRs, core-shell anatase/rutile phase
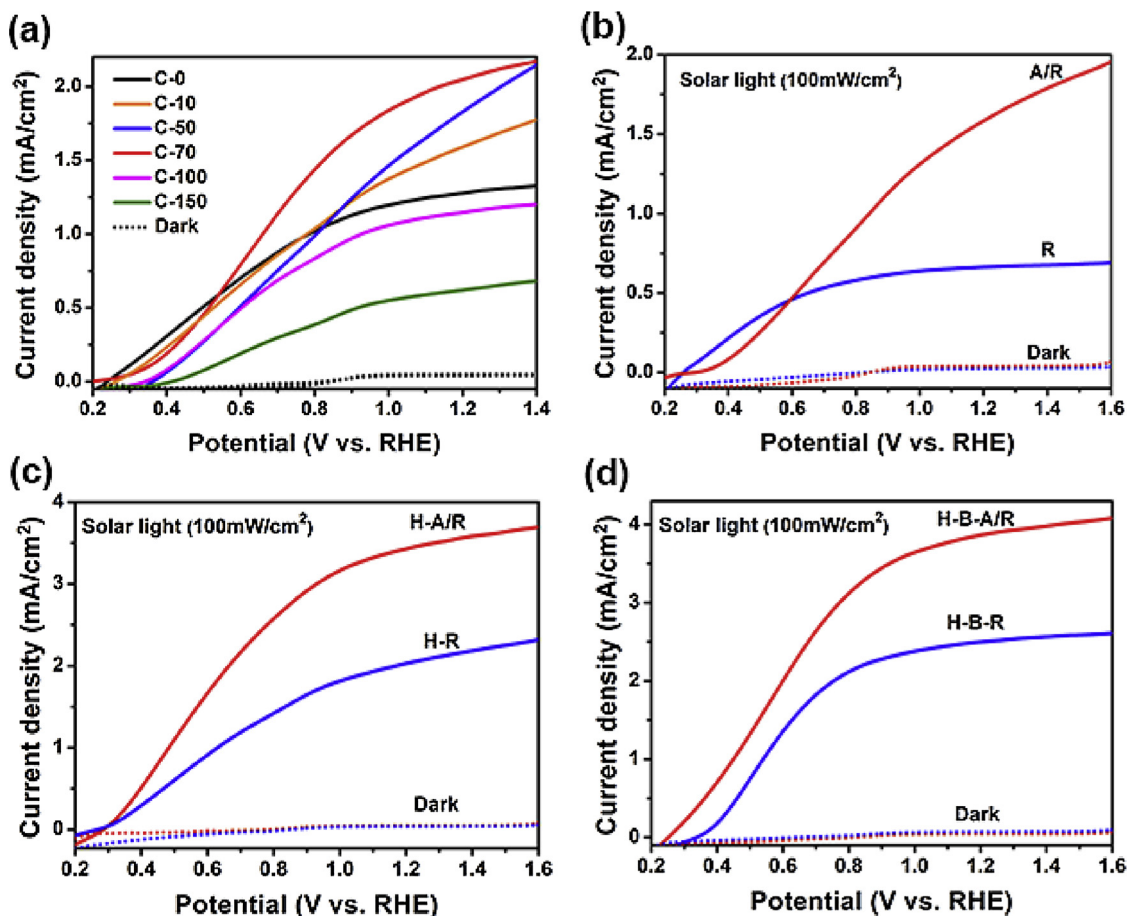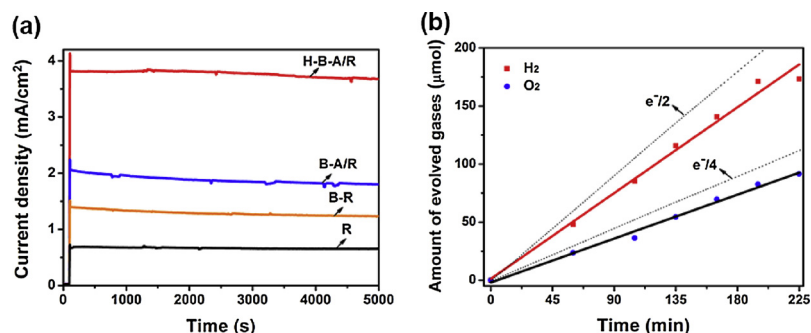

Fig. 7. Linear sweep voltammograms of branched rutile TiO_2 NRs with different ALD cycles from 10 times to 150 times (a), smooth rutile TiO_2 NRs with and without the anatase phase (b) followed by hydrogenated treatment (c), and hydrogenated branched rutile TiO_2 NRs with and without the anatase phase.

Fig. 8. (a) Stability tests of the as-obtained samples. (b) Amounts of oxygen and hydrogen evolved from the hydrogenated anatase/rutile phase heterojuncture branched TiO_2 NR photoanodes, as determined by gas chromatography. The experiments were carried out at 1.23 $V_{vs.RHE}$ under simulated solar light at 100 mW cm^{-2}.

heterojuncture branched TiO_2 NRs, and hydrogenated core-shell anatase/rutile phase heterojuncture branched TiO_2 NRs at 1.23 $V_{vs.RHE}$ under simulated solar light for long-term stability testing. The four curves remained steady without decay over the measurement period; this result indicates the good stability of the samples under simulated solar light. The core-shell phase heterojuncture branched TiO_2 NRs exhibited almost 86.5% of the initial photocurrent density of about 2.08 mA cm^{-2} and suggests that the core-shell phase heterojuncture with unique band structure and high built-in potential can suppress the recombination of photogenerated electron and hole pairs. In particular, the hydrogenated core-shell phase heterojuncture branched TiO_2 NRs manifested almost 94.8% of the original photocurrent density of about 3.88 mA cm^{-2} for 5000 s. This result indicates that introducing a disordered structure and oxygen vacancy within the energy band of the phase heterojuncture efficiently improves the active transport of photoinduced charge carriers and prohibit the recombination pathways. These results show that the synergy of the unique band structure of the anatase/rutile phase heterojuncture, the disordered layer on the samples, the oxygen vacancy after hydrogenated treatment, and the branched structure can significantly afford all samples with the desired stability.

The H_2 and O_2 evolution reaction was tested to verify whether the photocurrent

of the hydrogenated core-shell phase heterojuncture branched TiO_2 NR photoanode derives from water splitting rather than any other undesired side reactions. Fig. 8b shows the time courses of H_2 and O_2 evolution for the H-B-A/R at 1.23 $V_{vs.RHE}$ under the simulated solar light of 100 mW cm^{-2} in 0.1 M NaOH solution. The average H_2 and O_2 evolution rates were calculated to be approximately 49.2 and 25.2 μmol h^{-1} cm^{-2}, respectively, which were to the stoichiometric value of 2.0. The Faradaic efficiencies for H_2 and O_2 production were 68% and 70%, respectively. These values indicate that the photocurrent of the sample indeed originated from the hydrogen and oxygen evolution reactions, except for the possible contribution of water formation from the produced H_2 and O_2 in the present single-compartment cell. Thus, the hydrogenated core-shell phase heterojuncture branched TiO_2 NRs with enhanced PEC properties and excellent stability can be applied for the efficient reduction and oxidation of water under solar light.

An appropriate PEC water-splitting mechanism and the schematic

for the transfer route of photogenerated charge carriers in the H-B-A/R NRs are illustrated in Fig. 9. The enhanced efficient photoelectrochemical property can be attributed to the synergistic effect of the core-shell phase junction and highly ordered layer for fast charge separation and transmission rate, the branched and nanorod structure with large surface area for light-absorbing, and the post hydrogenated treatment with disorder surface layer and oxygen vacancy for the energy band modulation. Firstly, the single-phase TiO_2 NRs shows a poor PEC performance because of the high recombination rate of the photogenerated electron–hole pairs and low light absorption efficiency. However, the branched structure on the pure rutile TiO_2 NRs was introduced by the in situ chemical growth method and effectively improved the photocurrent density for the branched rutile TiO_2 NRs because of the enlarged specific surface area and light absorbance [12]. In particular, after a thin anatase phase layer was uniformly deposited on the surface of the branched rutile TiO_2 NRs, the branched anatase/rutile TiO_2 NRs was formed as core-shell phase heterojuncture photoelectrode, by ALD technique. As shown in Fig. 3c, the HRTEM image directly confirmed that the (101) and (004) lattice crystal planes of anatase TiO_2 grew in the conjunction with rutile TiO_2 on the TiO_2 NR trunk and branch surfaces. The unique energy band structure of 3.03 and 3.2 eV for the rutile and anatase phase, respectively, formed the high built-in potential within the anatase/rutile phase heterojunction and permitted the electrons to flow from the anatase into the rutile, with holes migrating in opposite directions [23,25,60–62]. This migration then efficiently increased the separation rate of photogenerated charge carriers and improved the PEC water-splitting properties. The photocurrent and stability further enhanced by the hydrogenated treatment in the hydrogenated core-shell phase heterojuncture branched TiO_2 NRs were mainly due to the disordered structure or oxygen vacancies (V_O) [42,48,53]. This lattice disorder can yield mid-gap states instead of forming discrete donor states, which can induce the merging of band tail states with the VB and CB edge [9]. These extended energy states, in combination with the energy levels, can become the dominant centers for optical excitation and relaxation. Besides, high-temperature hydrogen treatment creates surface hydroxyl group and oxygen vacancies (V_O) in the band gap of both anatase and rutile phases, which can improve the electrical conductivity and provide additional charge carriers [53]. Energy levels of oxygen vacancies have been reported to be about 0.75 and 1.18 eV below the CB of the hydrogenated TiO_2
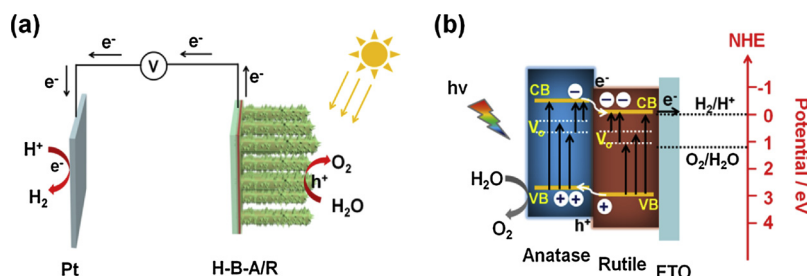
Fig. 9. Schematic for (a) the proposed mechanism of PEC water splitting and (b) the energy band structure of the hydrogenated anatase/rutile branched TiO_2 NRs.

[38,50]. Therefore, the electron transitions from the VB to the V_O levels or from the V_O to the CB contributed to the visible and near-infrared light absorption [49]. Moreover, the disordered structure and oxygen vacancies all notably appeared within the anatase and rutile phases after hydrogenation treatment. The synergistic effect of oxygen vacancies, disordered structure, and core-shell anatase/rutile phase heterojunction can further reduce the recombination rate of the photogenerated charge carriers and accelerate the transfer of electrons and holes. Thus, the hydrogenated core-shell anatase/rutile phase heterojunction branched TiO_2 NRs with enlarged specific surface area and light absorption, abundant hetero-interfaces, disordered structure, and oxygen vacancies efficiently facilitated the separation and migration of photoinduced electron and hole pairs. The fabricated nanorods also contributed to the enhanced PEC performance and water-splitting stability.

4. Conclusion

In summary, we demonstrated a new method to fabricate the hydrogenated TiO_2 phase heterojuncture with controllable core-shell structures (H-B-A/R) as photoanode for efficient PEC water splitting. This anatase/rutile phase heterojunction material showed a larger photocurrent density of 3.88 mA cm^{-2} and an IPCE value of 59.7% at 380 nm, which are almost 4.8 and 7.4 times than that of bare rutile TiO_2 respectively. Moreover, a high H_2 evolution rates of 49.2 μmol h^{-1} cm^{-2} was also achieved indicating that the hydrogenated phase heterojunction could be applied for the efficient reduction and oxidation of water under solar light, owing to the synergistic effect of the core-shell phase junction and highly ordered layer for fast charge separation and transmission rate, the branched and nanorod structure with large surface area for light-absorbing, and the post hydrogenated treatment with disorder surface layer and oxygen vacancy for the energy band modulation of TiO_2. Meanwhile, the H-B-A/R photocatalyst showed good photo-stability in long term, which imparts potential applications in photoelectrochemical water splitting, photocatalysis, solar cells, and other devices.

Acknowledgements

Appendix A. Supplementary data

Supplementary material related to this article can be found, in the online version, at doi:https://doi.org/10.1016/j.apcatb.2018.11.078.

References

[1] A. Fujishima, K. Honda, Nature 238 (1972) 37–38.
[2] K. Maeda, K. Teramura, D. Lu, T. Takata, N. Saito, Y. Inoue, K. Domen, Nature 440 (2006) 295.
[3] P. Roy, S. Berger, P. Schmuki, Angew. Chem. Int. Ed. 50 (2011) 2904–2939.
[4] K. Zhu, N.R. Neale, A. Miedaner, A.J. Frank, Nano Lett. 7 (2007) 69–74.
[5] X. Chen, S.S. Mao, Chem. Rev. 38 (2007) 2891–2959.
[6] S.U.M. Khan, M. Alshahry, W. B. I Jr., Science 297 (2002) 2243–2245.
[7] J. Zhang, Q. Xu, Z. Feng, M. Li, C. Li, Angew. Chem. Int. Ed. 47 (2008) 1766–1769.
[8] B. Liu, E.S. Aydil, J. Am. Chem. Soc. 131 (2009) 3985–3990.
[9] X. Chen, L. Liu, P.Y. Yu, S.S. Mao, Science 331 (2011) 746–750.
[10] R. Asahi, T. Morikawa, T. Ohwaki, K. Aoki, Y. Taga, Science 293 (2001) 269–271.
[11] M. Xu, P. Da, H. Wu, D. Zhao, G. Zheng, Nano Lett. 12 (2012) 1503–1508.
[12] I.S. Cho, Z. Chen, A.J. Forman, D.R. Kim, P.M. Rao, T.F. Jaramillo, X. Zheng, Nano Lett. 11 (2011) 4978–4984.
[13] T. Zhang, S. Cui, B. Yu, Z. Liu, D. Wang, Chem. Commun. 51 (2015) 16940–16943.
[14] M.R. Hoffmann, W. Choi, D.W. Bahnemann, Chem. Rev. 95 (1995) 69–96.
[15] Y.J. Hwang, C. Hahn, B. Liu, P.D. Yang, ACS Nano 6 (2012) 5060–5069.
[16] R. Tanwar, B. Kaur, U.K. Mandal, Appl. Catal. B: Environ. 211 (2017) 305–322.
[17] R. Tanwar, S. Kumar, U.K. Mandal, J. Photochem. Photobiol. A: Chem. 333 (2017) 105–116.
[18] R. Li, Y. Weng, X. Zhou, X. Wang, Y. Mi, R. Chong, H. Han, C. Li, Energy Environ. Sci. 8 (2012) 2377–2382.
[19] S.J.A. Moniz, S.A. Shevlin, D.J. Martin, Z.X. Guo, J. Tang, Energy Environ. Sci. 8 (2015) 731–759.
[20] M. Wang, L. Sun, Z. Lin, J. Cai, K. Xie, C. Lin, Energy Environ. Sci. 6 (2013) 1211–1220.
[21] H. Wang, Y. Bai, H. Zhang, Z. Zhang, J. Li, L. Guo, J. Phys. Chem. C 114 (2010) 16451–16455.
[22] L.W. Yin, R. Tang, J. Mater. Chem. A 3 (2015) 17417–17425.
[23] T. Kawahara, Y. Konishi, H.T. Dr, N.T. Dr, J. Nishii, S.I. Dr, Angew. Chem. Int. Ed. 114 (2002) 2935–2937.
[24] Z. Liu, X. Zhang, S. Nishimoto, M. Jin, D.A. Tryk, T. Murakami, A. Fujishima, Langmuir 23 (2007) 10916–10919.
[25] D. Tsukamoto, Y. Shiraishi, Y. Sugano, S. Ichikawa, S. Tanaka, T. Hirai, J. Am. Chem. Soc. 134 (2012) 6309–6315.
[26] Y.P. Yuan, L.W. Ruan, J. Barber, S.C.J. Loo, C. Xue, Energy Environ. Sci. 7 (2014) 3934–3951.
[27] P. Yan, X. Wang, X. Zheng, R. Li, J. Han, J. Shi, A. Li, Y. Gan, C. Li, Nano Energy 15 (2015) 406–412.
[28] H. Sutiono, A.M. Tripathi, H.M. Chen, C.H. Chen, W.N. Su, L.Y. Chen, H.J. Dai, B.J. Hwang, ACS Sustain. Chem. Eng. 4 (2016) 5963–5971.
[29] D.C. Hurum, A.G. Agrios, S.E. Crist, K.A. Gray, T. Rajh, M.C. Thurnauer, J. Electron Spectrosc. 150 (2006) 155–163.
[30] D.C.H. And, K.A. Gray, T.R. And, M.C. Thurnauer, J. Phys. Chem. B 109 (2016) 977–980.
[31] D.C. Hurum, A.G. Agrios, K.A. Gray, T. Rajh, M.C. Thurnauer, J. Phys. Chem. B 107 (2003) 4545–4549.
[32] Y. Cao, T. He, Y. Chen, Y. Cao, J. Phys. Chem. 114 (2017) 3627–3633.
[33] V. Etacheri, M.K. Seery, S.J. Hinder, S.C. Pillai, Chem. Mater. 22 (2010) 3843–3853.
[34] K. Shimura, H. Yoshida, Energy Environ. Sci. 4 (2011) 2467–2481.
[35] C. Wang, X. Zhang, C. Shao, Y. Zhang, J. Yang, P. Sun, X. Liu, H. Liu, Y. Liu, T. Xie, J. Colloid Interf. Sci. 363 (2011) 157–164.
[36] W.K. Wang, J.J. Chen, X. Zhang, Y.X. Huang, W.W. Li, H.Q. Yu, Sci. Rep. 6 (2016) 20491–20500.
[37] F. Fabregat-Santiago, E.M. Barea, J. Bisquert, G.K. Mor, K. Shankar, C.A. Grimes, J. Am. Chem. Soc. 130 (2008) 11312–11316.
[38] D.C. Cronemeyer, M.A. Gilleo, Phys. Rev. 82 (1951) 975–976.
[39] X. Sheng, D. He, J. Yang, K. Zhu, X. Feng, Nano Lett. 14 (2014) 1848–1852.
[40] J. Shi, Y. Hara, C. Sun, M.A. Anderson, X. Wang, Nano Lett. 11 (2011) 3413–3419.
[41] F. Zuo, L. Wang, T. Wu, Z. Zhang, B. Dan, P. Feng, J. Am. Chem. Soc. 132 (2010) 11856–11857.
[42] S. Hoang, S.P. Berglund, N.T. Hahn, A.J. Bard, C.B. Mullins, J. Am. Chem. Soc. 134 (2012) 3659–3662.
[43] A. Murphy, P. Barnes, L. Randeniya, I. Plumb, I. Grey, M. Horne, J. Glasscock, Int. J. Hydrogen Energ. 31 (2006) 1999–2017.
[44] V.E. Henrich, R.L. Kurtz, Phys. Rev. B 23 (1981) 6280–6787.
[45] H. Tang, K. Prasad, R. Sanjines, P.E. Schmid, F. Levy, J. Appl. Phys. 75 (1994) 2042–2047.
[46] H. Tang, F. Levy, H. Berger, P.E. Schmid, Phys. Rev. B 52 (1995) 7771–7774.
[47] E. Finazzi, C.D. Valentin, G. Pacchioni, A. Selloni, J. Chem. Phys. 129 (2008) 154113.
[48] G. Wang, H. Wang, Y. Ling, Y. Tang, X. Yang, R.C. Fitzmorris, C. Wang, J.Z. Zhang, Y. Li, Nano Lett. 11 (2011) 3026–3033.
[49] W. Kim, C. Kim, Q.W. Choi, Phys. Rev. B 30 (1984) 3625–3628.
[50] D.C. Cronemeyer, Phys. Rev. 113 (1959) 1222–1226.
[51] F.J. Knorr, C.C. Mercado, J.L. Mchale, J. Phys. Chem. C 112 (2008) 12786–12794.
[52] J. Ng, S. Xu, X. Zhang, Y.Y. Hui, D.D. Sun, Adv. Funct. Mater. 20 (2010) 4287–4294.
[53] A. Naldoni, M. Allieta, S. Santangelo, M. Marelli, F. Fabbri, S. Cappelli, C.L. Bianchi, R. Psaro, V. Dal Santo, J. Am. Chem. Soc. 134 (2012) 7600–7603.
[54] M.S. Lazarus, T.K. Sham, Chem. Phys. Lett. 92 (1982) 670–674.
[55] G. Li, N.M. Dimitrijevic, L. Chen, J.M. Nichols, T. Rajh, K.A. Gray, J. Am. Chem. Soc. 130 (2008) 5402–5403.
[56] Y. Yan, M. Han, A. Konkin, T. Koppe, D. Wang, T. Andreu, G. Chen, U. Vetter, J.R. Morante, P. Schaaf, J. Mater. Chem. A 2 (2014) 12708–12716.
[57] X.D. Jiang, Y.P. Zhang, J. Jiang, Y. Rong, Y.C. Wang, Y.C. Wu, C.X. Pan, J. Phys. Chem. C 116 (2012) 22619–22624.
[58] E. Mccafferty, J.P. Wightman, Surf. Interface Anal. 26 (2015) 549–564.
[59] S. Li, J. Qiu, M. Ling, F. Peng, B. Wood, S. Zhang, ACS Appl. Mater. Inter. 5 (2013) 11129–11135.
[60] J.X. Low, J.G. Yu, M. Jaroniec, S. Wageh, A.A. AlGhamdi, Adv. Mater. 29 (2017) 1601694.
[61] J. Liu, X.L. Yu, Q.Y. Liu, R.J. Liu, X.K. Shang, S.S. Zhang, W.H. Li, W.Q. Zheng, G.J. Zhang, H.B. Cao, Z.J. Gu, Appl. Catal. B: Environ. 158–159 (2014) 296–300.
[62] D.Y.C. Leung, X.L. Fu, C.F. Wang, M. Ni, M.K.H. Leung, X.X. Wang, X.Z. Fu, ChemSusChem 3 (2010) 681–694.